

Real-Contact Area Between an Elastomer and a Flat Plane Observed by Surface Plasmon Resonance: Optical Model Calculations

Satoru Maegawa¹ · Hiroshige Matsuoka¹ · Shigehisa Fukui¹ · Fumihiro Itoigawa² · Takashi Nakamura²

Received: 16 July 2016 / Accepted: 16 August 2016 / Published online: 30 August 2016
© Springer Science+Business Media New York 2016

Abstract This study presents a novel method for high-sensitivity measurement of the area of the real contact between an elastomer surface and a rigid flat plane, using the surface plasmon resonance (SPR) technique in the Kretschmann configuration. Through numerical calculations, the sensitivity of the SPR method for determining the real-contact area is discussed and compared to other typical optical techniques, such as total internal reflection and multiple beam optical interference. The wavelength dependence of the optical reflectance is simulated, as well as its change with the elastomer-plane gap thickness and the optical properties of the gap material. Non-transparent elastomers are also studied. Consequently, it was found that the SPR method has the highest sensitivity for the measurement of real-contact area; it can detect, for example, an ultra-thin air gap (or water gap) formed between the contacting surfaces from the measurement of the intensity of reflected light from the contact region.

Keywords Real-contact area · Surface plasmon resonance · Soft elastomer · Kretschmann configuration

List of Symbols

E^{in} Amplitude of the incident light electric field
 E^{out} Amplitude of the reflected light electric field

E^+ Resultant electric vector of all positive-going light waves
 E^- Resultant electric vector of all negative-going light waves
 N Complex refractive index
 R Reflectance
 ΔR Difference in reflectance
 h Gap thickness
 h_{max} Maximum gap thickness
 l_d Characteristic decay length of evanescent electromagnetic field
 m Sensitivity factor
 n Refractive index
 n_{eff} Effective refractive index
 Δn_{eff} Difference in effective refractive index
 r^{eff} Effective reflection coefficient
 r Fresnel reflection coefficient
 k Extinction coefficient
 β Phase change
 θ Incident angle
 λ Wavelength
 λ_{SPR} Resonance wavelength in the reflectance spectrum in the SPR method
 λ_{OIF} Peak wavelength in the reflectance spectrum in the OIF method

✉ Satoru Maegawa
maegawa@damp.tottori-u.ac.jp

¹ Department of Mechanical and Aerospace Engineering, Tottori University, 4-101 Minami, Koyama, Tottori 680-8553, Japan

² Department of Mechanical Engineering, Nagoya Institute of Technology, Gokiso-cho, Showa-ku, Nagoya, Aichi 466-8555, Japan

1 Introduction

In situ and real-time measurement of the area of real contact on a sliding surface is a powerful method for understanding the mechanism of friction, because the total area of real contact directly affects the magnitude of the friction force. Over the last several decades, a number of techniques that can determine the real-contact area have

been developed. These are based on several different principles, for example, optical methods based on interferometry and total internal reflection [1–8], contact resistance measurement methods [9–11], and ultrasonic-sensing methods [12, 13].

Among these, optical methods have been the most widely used for observation of the dynamics at the contact interface, because these methods can provide a direct measurement of spatio-temporal changes of the distribution of real-contact regions within an apparent contact area with high space and time resolution. A number of interesting phenomena have been discovered and closely investigated by optical measurements, for example, the dynamic propagation of precursory partial slippage that occurs prior to the onset of global slip [14, 15], and the unique dynamics for a sliding surface made of soft materials, resulting in Schallamach wave propagation [16–18]. On the other hand, optical methods have some limitations on material transparency; for example, one contacting surface should be made of a transparent material, such as glass, acrylic, or silicon resin. However, for the simplicity of construction and data analysis, optical methods have become one of the most useful experimental techniques for the study of friction.

In this study, as an alternative optical technique for the direct observation of real-contact area, a novel method is introduced, based on observing surface plasmon resonances (SPR) in the Kretschmann configuration. As far as the authors know, the application of SPR for real-contact area measurement has not been previously addressed. Numerical calculations based on multi-layer optical models indicate that the SPR method proposed here has a high sensitivity for detecting real-contact area distributed within an apparent contact region, in comparison with other optical methods based on total internal reflection (TIR) or optical interference (OIF). It was found from the model that SPR methods can detect an ultra-thin gap layer of a few nanometers thickness without any special calibration or analysis.

2 Optical Models

This study focused on three different optical methods that can directly detect separated small real-contact regions distributed within the apparent contact area. One is the surface plasmon resonance method, and the others are a total internal reflection method and an optical interference method. As described in the introduction, this study is the first to use the potential of the SPR method for real-contact area observations. Optical models of these measurement methods are schematically illustrated, as shown in Figs. 1, 2 and 3. Roughly speaking, their basic configurations are

similar, and all the methods are based on monitoring a reflected light intensity. The basic elements are, therefore, an incident light source, a contact interface as the measured object, and a detector for the reflected light intensity.

The particular aim of this study is to evaluate the measurement sensitivity for real-contact area, using the SPR method. A particular elastomer, polydimethylsiloxane (PDMS), was chosen as the reference condition to facilitate the comparison of numerical results for the three different methods. In addition, it should be noted that a simplified polarization analysis will be used for discussion purposes, although a full polarization analysis may reveal potential improvements in the measurement sensitivity of each method. Therefore, a *p*-polarized incident light source will be considered, as *p*-polarized light is necessary to trigger surface plasmons (SPs); *s*-polarized light is ineffective. Furthermore, it should also be noted, as is well known, that SPs can be excited on only a limited number of metal surfaces. Basically, only Au, Ag, Cu, and Al can be used for SPs triggered by visible light. In this study, Au was used for the model calculation, because it has the highest SPR response compared to the other metals listed.

In the previous research, the authors discussed the application of the SPR method to the measurement of lubricant film thickness [19]. In that report, SPR in the Otto configuration was considered, while in the current study, the Kretschmann configuration was used to measure real-contact area. In the Otto configuration [20], the surface plasmon is excited on the surface of bulk metal, which is separated from a glass prism by a thin gap of air or dielectric with a thickness of a few hundred nm. In contrast, in the Kretschmann configuration [21], the SP is excited on a thin metal film (thickness of several tens of nm) deposited on a glass prism. The difference between these two different configurations is described in many references, for example [22]. In general, SPR measurements in the Kretschmann configuration are more common in biological studies, because the construction of the system is relatively simple. In the case of the Otto configuration, a careful adjustment of the gap thickness between the glass prism and the metal surface is needed to trigger the SP.

Figure 1 shows the optical model of the SPR method. Figure 1a shows an overview of the optical system, and Fig. 1b shows a magnified view within the apparent contact region. This model is composed of a transparent half-cylinder glass prism made of SF11 (a flint glass with high refractive index $n \approx 1.8$), a Au thin film with a thickness of 48 nm deposited on the bottom face of the prism, an elastic hemisphere made of PDMS with a rough surface, a gap that separates the surfaces of the Au film and the PDMS hemisphere, and other optical components, including a *p*-polarized white light source and a light detector.

Fig. 1 Schematics of the optical model of the surface plasmon resonance (SPR) method discussed in this study: **a** overview of the optical system; **b** magnified view of the real-contact regions, spatially distributed within the apparent contact area

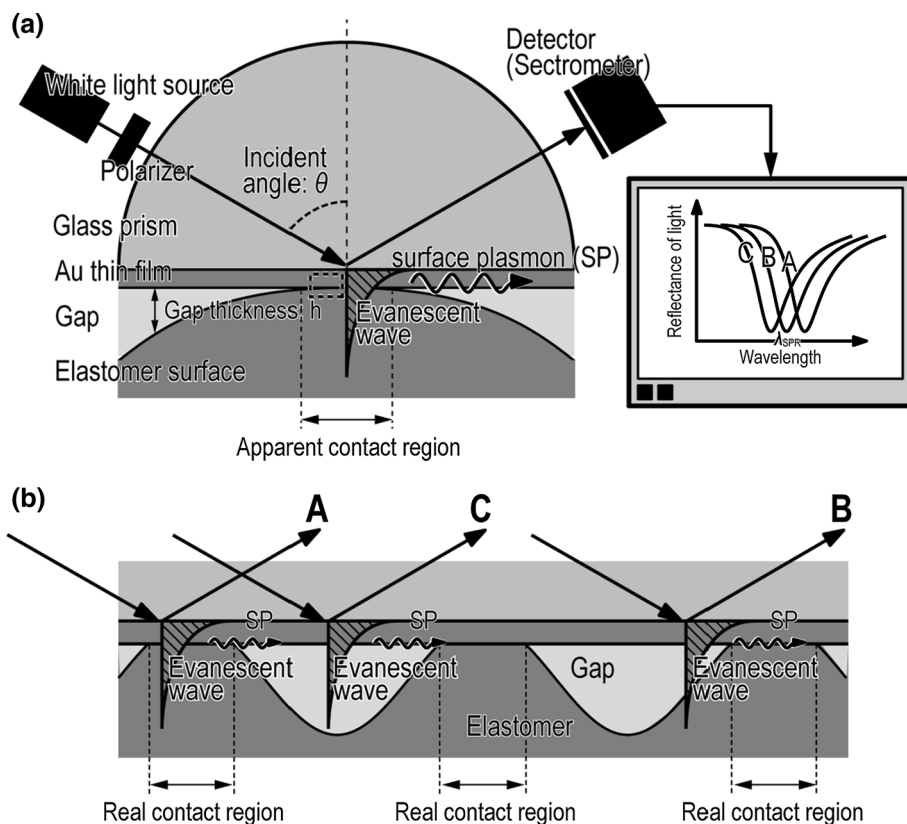
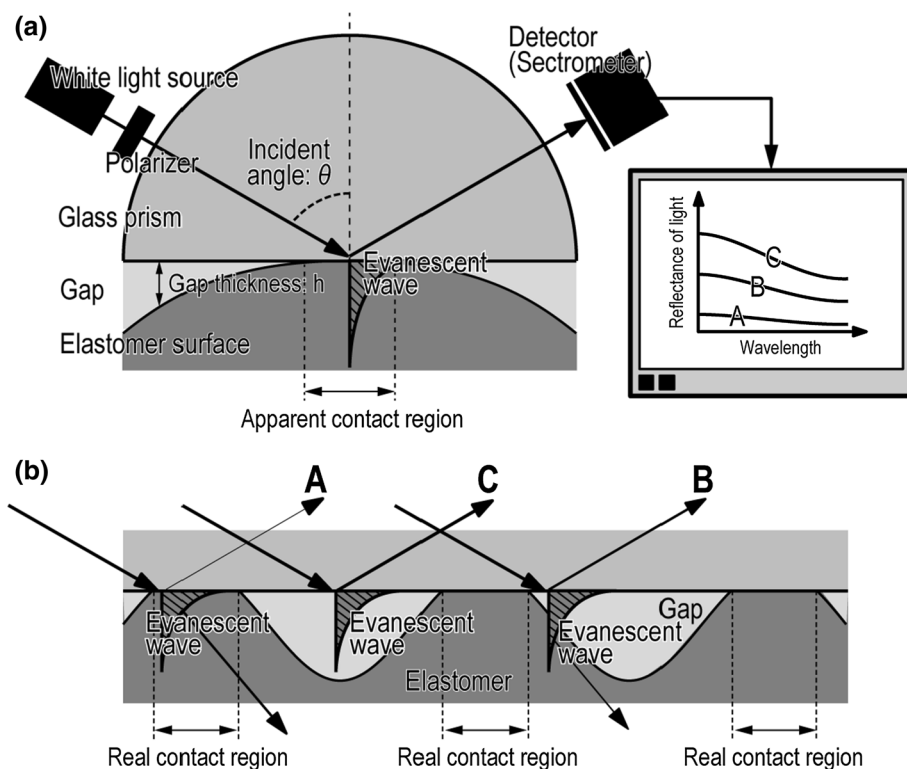


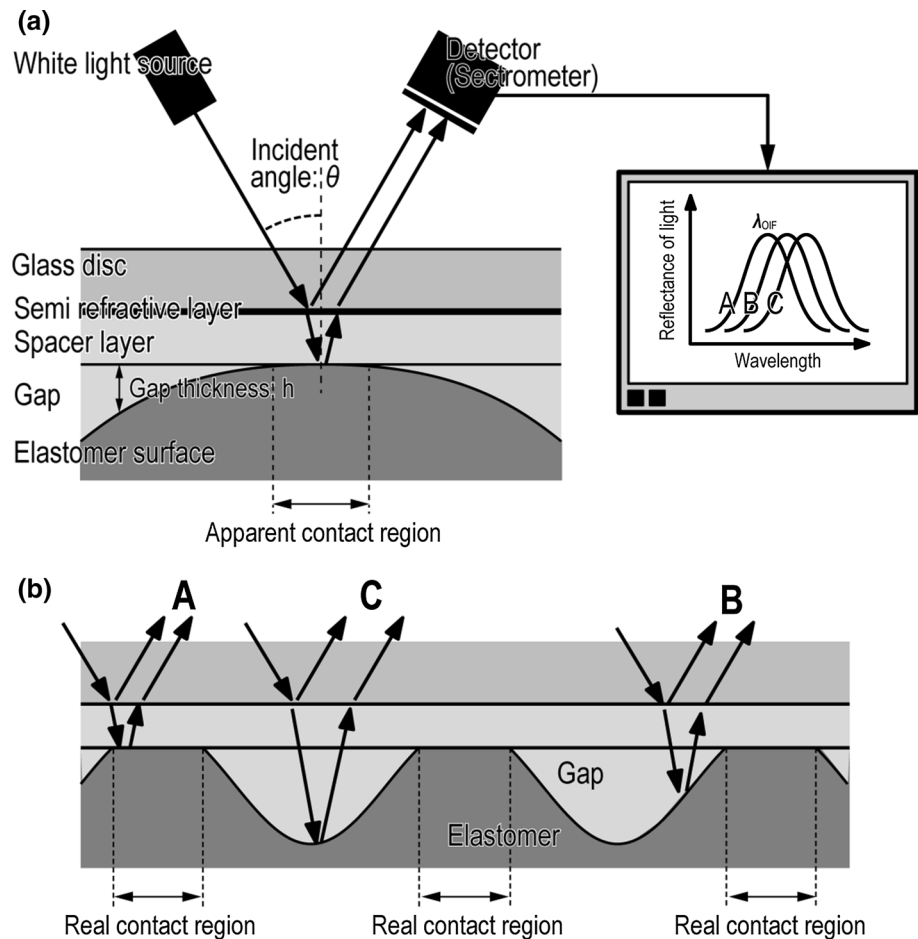
Fig. 2 Schematics of the total internal reflection (TIR) method: **a** overview of the optical system; **b** magnified view of the real-contact regions



Thus, the system creates a “point” contact between the PDMS hemisphere and the Au thin film, in which a number of tiny real-contact regions are formed, as shown in

Fig. 1b. The *p*-polarized white light is reflected at the bottom face of the prism, as denoted in the arrows in Figs. 1a and b. The incidence angle of the light θ_{SPR} is set

Fig. 3 Schematics of the optical interferometry (OIF) method: **a** overview of the optical system; **b** magnified view of the real-contact regions



to be larger than the critical angle for total reflection, i.e., in this study, $\theta_{\text{SPR}} = 58^\circ$. An evanescent electromagnetic wave is formed near the reflecting plane, as shown by the hatched area in the figure. The intensity of the evanescent field decays exponentially with increasing distance from the reflecting plane. When the wave vector of the evanescent electromagnetic field matches the SP wave vector, an SP is excited on the surface of the Au thin film. When an SP is triggered, some of the light energy is transformed into SP energy. Therefore, the light reflectance spectrum has a minimum at the resonance wavelength λ_{SPR} , as illustrated in Fig. 1a.

As will be discussed in following sections, the resonance wavelength λ_{SPR} shows great sensitivity to small changes in the gap h . For the light path “A” in Fig. 1b, at a real-contact point, where $h = 0$, all the evanescent light fields are located in the bulk region of the elastomer. On the other hand, in non-contact regions, e.g., light path “C”, where $h \neq 0$, the evanescent light field is localized in the gap. In the case of a region with a sufficiently small gap thickness, e.g., light path “B”, there is an evanescent field in the gap medium, and also in the bulk elastomer. The resonance wavelength λ_{SPR} strongly depends on the effective

refractive index in the evanescent field [23]. The dependence of λ_{SPR} is illustrated in the spectrum in Fig. 1a; λ_{SPR} for “C” is smaller than for “B” or “A.” Thus, λ_{SPR} decreases with increasing gap thickness h . The h dependence of λ_{SPR} means that the spatial distributions of the real-contact area regions can be visualized by monitoring the reflected light intensity profile. It should be noted that the magnitude of the h dependence of λ_{SPR} is a function of the refractive index discrepancy between the gap material and the elastomer, as explained in a latter section.

Figure 2 illustrates the optical model of a typical total internal reflection method. From a comparison of Figs. 1a and 2a, it is clear that the optical configurations for these methods are quite similar. In the case of TIR, there is no Au thin film (as used in the SPR method), because excitation of an SP is not required. It should be noted that a typical optical glass (BK7, a borosilicate crown glass with $n \approx 1.5$) is used for the prism in the TIR model. The remainder of the TIR configuration is the same as for the SPR method.

In the TIR method, as with SPR, the intensity of the reflected light depends on h , and the spatial distribution of the real-contact regions can be observed by monitoring the

reflected light profile. The mechanism of the h dependence of the reflected light intensity is schematically shown in Fig. 2b, which indicates that the spatial distribution of real-contact regions formed within the apparent contact region. In a real-contact region (i.e., $h = 0$, illustrated by path “A” in the figure), there is little internal reflection, because the difference of the refractive indexes of BK7 glass and PDMS elastomer, $n \approx 1.4$, is quite small. In contrast, in regions, where a large enough gap h is formed, there is a relatively large reflection (illustrated by line “C” in the figure), because the BK7-gap refractive index difference is larger than for BK7 elastomer. In the other regions, where the gap layer is of an intermediate thickness, some light is reflected and the remainder is transmitted into the bulk of the PDMS hemisphere, (illustrated by line “B” in the figure). Therefore, the intensity of the reflected light depends on the magnitude of h . The h dependence of the reflectance spectrum is also illustrated in the spectra in Fig. 2a. Note that in this study, the incident angle θ_{TIR} is set to 58° , which is larger than the total internal reflection.

The optical configuration for the optical interference (OIF) method is shown in Fig. 3, and again is similar to the above two methods. The figure illustrates the beam paths for two-beam interference for simplicity; however, in the calculation that follows, multiple beam interference is considered. For both the two-beam and multiple beam models, the basic principle for detecting and measuring the existence and thickness of the gap thickness is identical. As illustrated in Fig. 3, the optical model for the OIF method consists of a transparent rectangular prism of BK7 glass, a Cr thin film with a thickness of 8 nm deposited on the bottom face of the prism (i.e., a semi-reflecting layer), an SiO₂ spacer layer, a PDMS elastic hemisphere with a rough surface, a gap layer between the bottom face of the SiO₂ layer and the PDMS hemisphere, and other optical components, including a p -polarized white light source and a light detector. The beam-splitting Cr layer is needed to create optical interference between two different beam paths, as shown in the figure.

Similar to the other cases, the intensity of the reflected light depends on h in this case, because it affects the interference pattern. A white light beam is shone onto the contact region. The beam is split by the semi-reflective layer, some light being reflected, and some passing through the spacer and gap layers, and then being reflected from the top face of the PDMS surface. The reflected beams are recombined, with the path difference depending on the sum of the optical path lengths through the spacer layer and the gap. Because the spacer layer thickness is known in advance, changes in the gap thickness can be determined by the measured shift of the peak position λ_{OIF} in the interference spectrum. The h dependence of the beam paths

is schematically illustrated in Fig. 3a. Note that, in this study, the incident angle θ_{OIF} is set to zero.

3 Model Calculations

3.1 Multiple Beam Interference Model

As illustrated in Figs. 1, 2 and 3, in all the methods discussed in this study, the sensitivity for the measurement of real-contact area is determined by the sensitivity of the reflected light intensity to changes in h . This section shows the theoretical techniques for calculating the wavelength dependence of the reflectance. The derivation of the following equations is found in many references [e.g., 24–26].

Figure 4 illustrates a basic model of multiple beam interference in multi-layered dielectric films. Figure 4a shows a schematic diagram of the multiple beam paths. Here, the optical properties of the layers are described using a complex refractive index N :

$$N_i = n_i - ik_i, \quad (1)$$

where n_i and k_i are the real refractive index and the extinction coefficient of the i th layer, respectively. For optically transparent materials, e.g., transparent glass, the extinction coefficient k is zero.

As shown in Fig. 4b, all the transmitted light in the i th layer and the reflected light at the interface between the i th and $i + 1$ th layers are represented by E_i^+ and E_i^- , respectively [27]. The arrows in Fig. 4b represent the direction of the electric field vectors. Here, $E_i^+ = \sum E_i^{\text{in}}$ and $E_i^- = \sum E_i^{\text{out}}$. Therefore, the effective reflection coefficient at the interface between the i th and $i + 1$ th layers r_i^{eff} can be written as

$$r_i^{\text{eff}} = E_i^- / E_i^+ \quad (2)$$

From the boundary conditions of continuity of electric and magnetic vectors at the interface of different layers, r_i^{eff} can be formulated as follows [24–26]:

$$r_{i-1}^{\text{eff}} = \frac{r_{i-1} + r_i^{\text{eff}} e^{-i2\beta_i}}{1 + r_{i-1} r_i^{\text{eff}} e^{-i2\beta_i}}, \quad (3)$$

where $\beta_i = 2\pi n_i h_i \cos \theta_i / \lambda$, h_i is the thickness of the i th layer, and λ is the wavelength of the incident light. In addition, r_{i-1} included in Eq. (3) is the Fresnel reflection coefficient, which is determined by

$$r_{i-1} = \frac{N_{i-1} \cos \theta_{i-1} - N_i \cos \theta_i}{N_{i-1} \cos \theta_{i-1} + N_i \cos \theta_i} \quad (4)$$

From Snell’s law, i.e., $n_0 \sin \theta_0 = n_1 \sin \theta_1 = n_2 \sin \theta_2 = \dots = n_i \sin \theta_i$, the incident angle at the interface θ_i can be written as

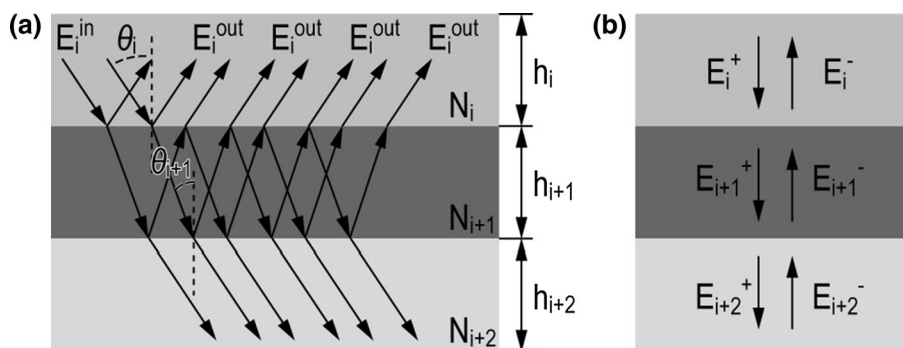


Fig. 4 Simplified multiple beam interference theory: **a** schematic illustration of the beam paths in multiple beam interference; two incoming beams represent a wavefront; multiple outgoing beams indicate multiple reflections; **b** effective model including the resultant electric vector of all positive-going and negative-going light waves,

$$\cos \theta_i = \sqrt{1 - \left(\frac{n_0}{n_i} \sin \theta_0\right)^2}, \tag{5}$$

where n_0 and θ_0 are the refractive index of the top layer of material and the incident angle at the interface between the top and second layers, respectively. From Eqs. (3)–(5), considering that the total reflectance R is described by the effective reflection coefficient at the top interface, i.e., $R = |r_0^{\text{eff}}|^2$, we can formulate the total reflectance R for the optical systems, as shown in Figs. 1, 2 and 3.

For example, in the case of the SPR method, which is described by a four-layer model, the reflectance R_{SPR} is given by

$$R_{\text{SPR}} = |r_0^{\text{eff}}|^2 = \left| \frac{r_0 + r_1^{\text{eff}} e^{-i2\beta_1}}{1 + r_0 r_1^{\text{eff}} e^{-i2\beta_1}} \right|^2, \tag{6}$$

where

$$r_1^{\text{eff}} = \frac{r_1 + r_2^{\text{eff}} e^{-i2\beta_2}}{1 + r_1 r_2^{\text{eff}} e^{-i2\beta_2}} \quad \text{and} \quad r_2^{\text{eff}} = r_2.$$

Here, layers 0–3 correspond to the SF11 prism, Au film, gap layer, and PDMS medium, respectively, and N_0 , N_1 , N_2 , and N_3 correspond to the complex refractive indexes of those layers. N are included in the reflectance R_{SPR} (Eq. 6) via Eq. (4). In addition, the gap thickness h corresponds to the thickness of the 2nd layer, i.e., h_2 .

Similarly, the total reflectances R_{TIR} and R_{OIF} of the TIR and OIF methods can be formulated using Eqs. (3)–(5). As illustrated in Figs. 2 and 3, the TIR model has three layers, while the OIF model has five.

3.2 Calculation Conditions

Table 1 and Fig. 5 show the materials used in the calculations, and their real refractive index n and extinction coefficient k . The wavelength dependence of the optical

i.e., E_i^+ and E_i^- . In **a** and **b**, arrows represent the direction of light propagation, while the E parameters represent the amplitudes of electric field vectors (in an appropriate direction, not shown)

properties of SF11, BK7, Au, Cr, and SiO_2 shown in Fig. 5 is based on [28]. As a reference condition, an air gap was considered. In addition, the following two cases are considered: contact between the flat surface and a PDMS elastomer, with a water gap; contact between the flat surface and an optically non-transparent ($k = 0.1$) elastomer, with an air gap. The water gap results are presented in Figs. 10, 11 and 12, and the non-transparent elastomer results in Figs. 13, 14 and 15.

In the SPR model, a high-refractive-index prism (SF11) is needed to trigger the occurrence of SP. In the other two methods, a typical lower index optical material (BK7) was used for the glass prisms. As is well known, the thickness of the Au layer strongly affects the SPR curve [22]. In this study, the thickness of the Au (48 nm) was determined, so that a large SPR response associated with the gap thickness h was indicated in the calculation. In addition, as pointed out in [27, 29], the optical properties and the thickness of the semi-reflective layer (i.e., the Cr layer) strongly affect the sensitivity of the OIF measurements. Therefore, the most frequently used material (Cr) was adopted, and the thickness of the Cr layer was determined in preliminary calculations.

4 Results

Figure 6 shows the model calculation results for the contact interface between a PDMS elastomer and a flat plane with air gaps. In the figure, calculated spectra of the reflected light for three methods, i.e., R_{SPR} , R_{TIF} , and R_{OIF} , are shown. It is found that the shape of the spectrum strongly depends on the thickness of the air gap h . It should be noted that the range of the air gap thickness h in the SPR calculation in Fig. 6a is smaller than in the other two methods (Fig. 6b, c).

Table 1 Optical properties used in model calculations

Material	n	k	h
SF11	Shown in Fig. 5	Shown in Fig. 5	–
BK7	Shown in Fig. 5	Shown in Fig. 5	–
Au	Shown in Fig. 5	Shown in Fig. 5	48 nm
Cr	Shown in Fig. 5	Shown in Fig. 5	8 nm
SiO ₂	Shown in Fig. 5	Shown in Fig. 5	–
Air	1.00	0	h
Water	1.33	0	h
PDMS	1.41	0	–
Elastomer (nontransparent)	1.41	0.1	–

Fig. 5 Optical characteristics of materials used for calculations: **a** real refractive index; **b** extinction coefficient

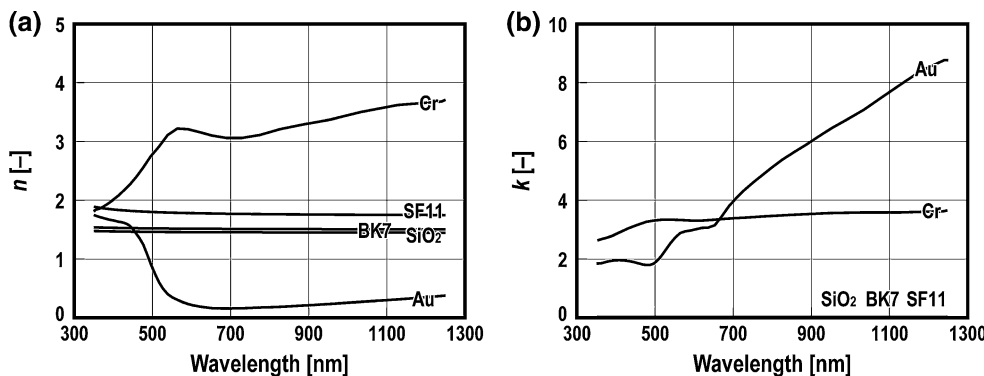
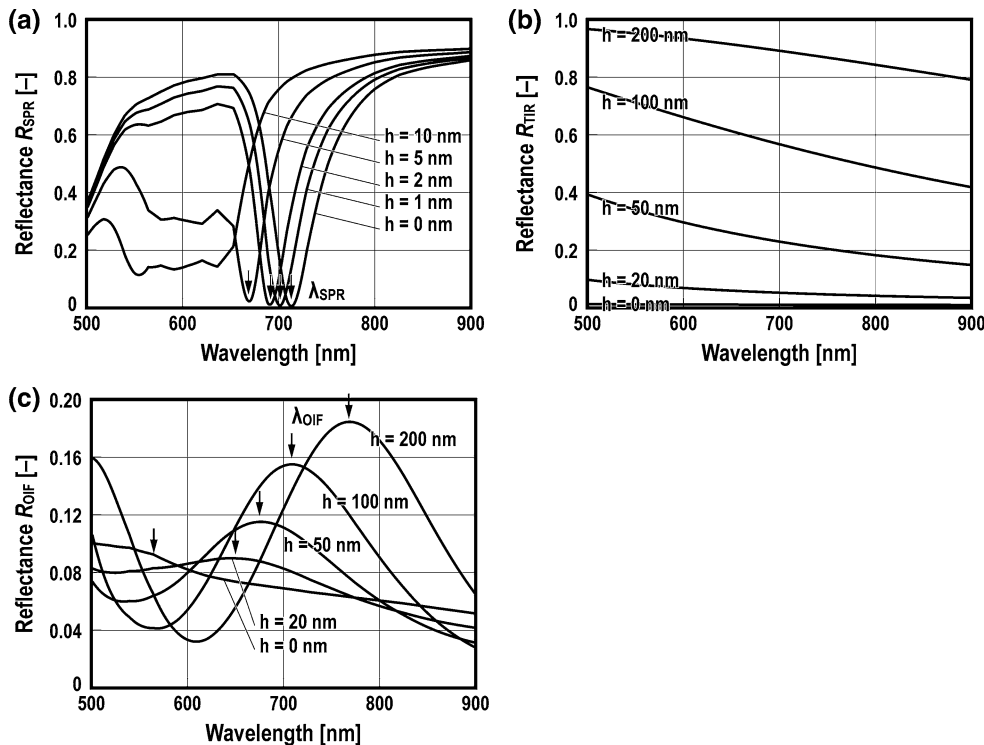


Fig. 6 air gap results: wavelength dependence of R_{SPR} , R_{TIR} , and R_{OIF} for contact between the PDMS elastomer and the flat plane with an air gap h : **a** SPR method; **b** TIR method; **c** OIF method. Arrows indicate a resonance or broad maximum in the response curve



For the SPR method, Fig. 6a, the position of λ_{SPR} (denoted by the arrows in the figure) shifts to lower wavelengths with increasing h . The shift is typical in SPR

measurements. The shift of λ_{SPR} is characterized by the changes in the effective refractive index on the evanescent field. Thus, different values of h work to vary the effective

refractive index at the contact region, leading to a shift in the position of λ_{SPR} . The relationship between the shift of λ_{SPR} and the air gap thickness h governs the sensitivity for the measurement of the real-contact area, which will be discussed in the following sections.

For the TIR method, Fig. 6b, the reflectance R_{TIR} at all wavelengths increases with increasing h . The mechanism of the change in R_{TIR} has already been explained in connection with Fig. 2b: when the gap h is relatively small, most of the incident light goes into the PDMS medium; when h is larger than the penetration depth of the evanescent wave, most of the incident light is reflected.

For OIF, the reflectance spectrum R_{OIF} also depends on h . In this case, the position of λ_{OIF} (which is defined as a broad maximum, and denoted by arrows in Fig. 6c) shifts to higher wavelengths with increased interfering path length differences. Furthermore, it is seen that the amplitude of the fluctuations in R_{OIF} also increases with h .

5 Discussion

5.1 Sensitivity for Detecting Real-Contact Regions

From the calculation results in Fig. 6, it was found that the magnitude and shape of the reflectance spectrum R depend on h for all three methods. In this study, the sensitivity for detecting the real-contact regions distributed within the apparent contact region is determined from the relationship between R and h .

Figure 7 shows the change of the reflectance with h , relative to the $h = 0$ nm case. Thus, for example, $\Delta R_{\text{SPR}}(725 \text{ nm})$ means $\Delta R_{\text{SPR}} = R_{\text{SPR}}(h) - R_{\text{SPR}}(h = 0 \text{ nm})$ at the wavelength of 725 nm. From Fig. 7, the sensitivity of R associated with the change in h under the SPR method is much larger than that under the other two methods, because the slope of the $\Delta R_{\text{SPR}}(725 \text{ nm})$

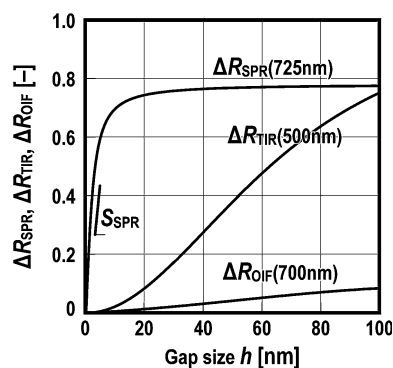


Fig. 7 Reflectance changes $\Delta R_{\text{SPR}}(725 \text{ nm})$, $\Delta R_{\text{TIR}}(500 \text{ nm})$, and $\Delta R_{\text{OIF}}(700 \text{ nm})$, associated with the gap size h for contact between the PDMS and flat plane via an air gap. The line S_{SPR} indicates the initial slope of ΔR_{SPR}

around $h = 0$ nm, which is denoted as S_{SPR} in Fig. 7, is much larger than that under the other methods. It means that the SPR method can detect the boundary between real-contact and non-contact regions more clearly. Thus, a large change in the reflectance can be observed, even if the thickness of the air gap is only a few nm. In contrast, in the case for TIR and OIF methods, it is relatively difficult to define the boundary between real-contact and non-contact regions from the measurement of reflected light intensity.

The high sensitivity of the SPR model is clearly seen in the model calculation (Fig. 8). The figure shows the spatial intensity profiles of $\Delta R_{\text{SPR}}(725 \text{ nm})$, $\Delta R_{\text{TIR}}(500 \text{ nm})$, and $\Delta R_{\text{OIF}}(700 \text{ nm})$ for a rough-contact surface, including regions of real contact and non-contact (upper illustrations in Fig. 8). Figures 8a, b differ in the maximum gap thickness h_{max} they portray; $h_{\text{max}} = 80$ nm in the former and 2 nm in the latter. It is clearly seen that the SPR method has the highest sensitivity to detect the real-contact regions. For $h_{\text{max}} = 80$ nm (Fig. 8a), the boundary between the real-contact and non-contact regions is clearly distinguishable from the reflected light intensity profile. For $h_{\text{max}} = 2$ nm (Fig. 8b), the SPR method can detect the non-contact regions, even if the thickness of the air gap is only on the order of a few nm. Thus, the model numerical calculations indicate that SPR provides a highly feasible method for distinguishing non-contact from contact regions.

It should be noted from Fig. 7 that $\Delta R_{\text{SPR}}(725 \text{ nm})$ linearly increases for small h , and then saturates. On the other hand, $\Delta R_{\text{TIR}}(500 \text{ nm})$ and $\Delta R_{\text{OIF}}(700 \text{ nm})$ linearly increase with h through the calculation range. Therefore, as shown in Fig. 8a, from the wide linear relationships between $\Delta R_{\text{TIR}}(500 \text{ nm})$ or $\Delta R_{\text{OIF}}(700 \text{ nm})$ and h , the gap thickness distribution can be measured by the profile of $\Delta R_{\text{TIR}}(500 \text{ nm})$ and $\Delta R_{\text{OIF}}(700 \text{ nm})$. However, for a much smaller h (Figs. 7, 8b), the profile of $\Delta R_{\text{SPR}}(725 \text{ nm})$ corresponds to the thickness distribution of the air gap because of the linear relationship with h .

As is well known, the change in $\Delta \lambda_{\text{SPR}}$ or ΔR is characterized by a change in the effective refractive index. As described above, the evanescent electromagnetic field decays exponentially into the bulk elastomer with a characteristic decay length, l_d , which is typically estimated as half of the light wavelength [23]; in the SPR model, l_d is thus approximately 350 nm. It should be noted that strictly speaking, l_d is not a constant value, it depends on the value of refractive index in the contact region and h . However, as shown in the following discussion, in this study, the relationship between ΔR_{SPR} and h under small h is analyzed. In this case, the h dependence of l_d is quite small. Therefore, in this study, it is assumed that l_d has a constant value, i.e., $l_d = 350$ nm. The effective refractive index in the contact region can be found [23] by averaging the refractive index

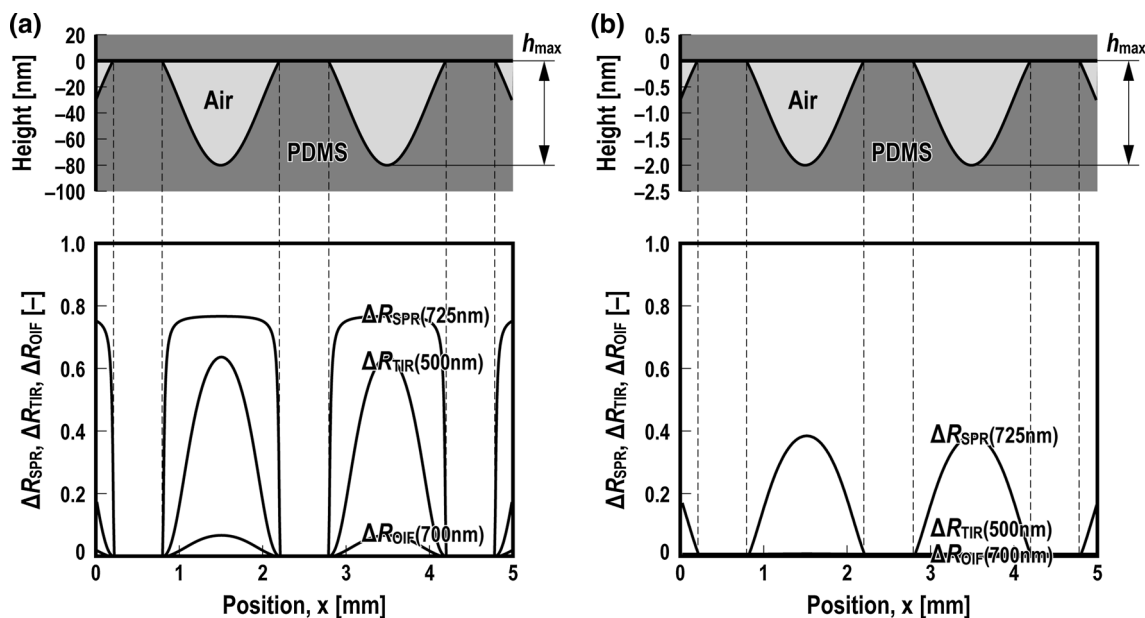


Fig. 8 Results of model calculations of the spatial distribution of ΔR_{SPR} , ΔR_{TIR} , and ΔR_{OIF} when the rough surface of an optically transparent PDMS elastomer is in contact with a flat rigid plane via air

gaps: **a** maximum gap between the flat and the elastomer surfaces is 80 nm; **b** maximum gap is 2 nm

over the evanescent field, using the field as weighting factor. Assuming a bilayer structure involving an air- or water-gap with thickness h (Fig. 9), n_{eff} can be written as

$$n_{eff} = (2/l_d) \int_0^\infty n(z) \exp(-2z/l_d) dz, \tag{7}$$

where $n(z)$ is the reflective index at depth z in Fig. 9. The refractive index is defined as $n(z) = n_{gap}$ in the air gap layer (i.e., $0 < z < h$), and $n(z) = n_{elastomer}$ in the bulk elastomer (i.e., $h \leq z < \infty$). Therefore, Eq. (7) can be reduced to

$$n_{eff} = n_{gap} [1 - \exp(-2h/l_d)] + n_{elastomer} \exp(-2h/l_d) \tag{8}$$

and further simplified:

$$n_{eff} = n_{elastomer} + (n_{gap} - n_{elastomer}) [1 - \exp(-2h/l_d)]. \tag{9}$$

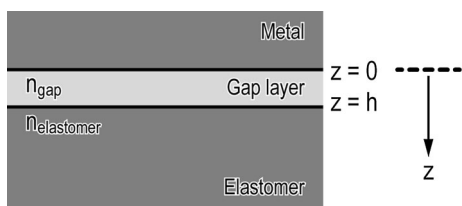


Fig. 9 Schematic diagram of a bilayer structure involving an air gap or water gap with thickness h

The SPR response for a small change in the effective refractive index is described as a following relationship [30]:

$$\Delta R_{SPR} = m \Delta n_{eff}, \tag{10}$$

where m is a sensitivity factor that depends on the system used, and Δn_{eff} is the change in n_{eff} . Considering that Δn_{eff} is the difference of the refractive indexes between the contact and non-contact conditions (gap thickness h), $\Delta n_{eff} = n_{eff}(h \neq 0) - n_{eff}(h = 0 \text{ nm})$ and Eq. (10) becomes

$$\Delta R_{SPR} = m(n_{gap} - n_{elastomer}) [1 - \exp(-2h/l_d)]. \tag{11}$$

For small values of h/l_d , Eq. (11) becomes

$$\Delta R_{SPR} = m(n_{gap} - n_{elastomer}) 2h/l_d, \tag{12}$$

and the initial slope S_{SPR} in Fig. 7 can now be formulated as $S_{SPR} = 2 m(n_{gap} - n_{elastomer})/l_d$. This shows that for small values of h/l_d , there is a linear relationship between ΔR_{SPR} and h . Thus, the thickness of an ultra-thin gap can be monitored using the reflected light intensity, as shown in Fig. 8a.

5.2 Sensitivity Under Water Lubrication Condition

As described in Eq. (12), the SPR sensitivity for determining non-contact regions is determined by the refractive index difference between the elastomer and the gap material, i.e., $n_{gap} - n_{elastomer}$. Figure 10 shows the wavelength dependence of $R_{SPR}(725 \text{ nm})$, $R_{TIR}(500 \text{ nm})$, and

$R_{OIF}(700\text{ nm})$ for a water film in the gap between the flat plane and the rough PDMS surface. These should be compared to Fig. 6, where an air gap was considered. Figures 11 and 12 show the relationship between ΔR and h and the model calculations, respectively, for a water gap. These correspond to Figs. 7 and 8, respectively, for the air gap.

From a comparison between Figs. 7 and 11, it is found that the sensitivity of the SPR method for a water gap is lower than for an air gap; in addition, the slope S_{SPR} in Fig. 11 is much smaller than in Fig. 7. This is a consequence of the effective refractive index appearing in Eq. (12): for an air gap, $n_{gap} - n_{elastomer} = 1.0 - 1.41 = -0.41$, while for a water gap, $n_{gap} - n_{elastomer} = 1.33 - 1.41 = -0.08$. For water lubrication conditions, Fig. 12 shows that it is relatively difficult to detect small gaps distributed within the apparent contact region. However, this study emphasizes that the sensitivity of the SPR method is nonetheless much higher than the other two methods, even when a water gap is formed in the apparent contact region.

5.3 Sensitivity When a Non-transparent Elastomer is Used

Figures 13, 14 and 15 show the calculations when a non-transparent elastomer ($k = 0.1$) is used. These are similar to Figs. 6, 7 and 8 in assuming an air gap. From a comparison of Figs. 6 and 13, it is found that the spectrum of

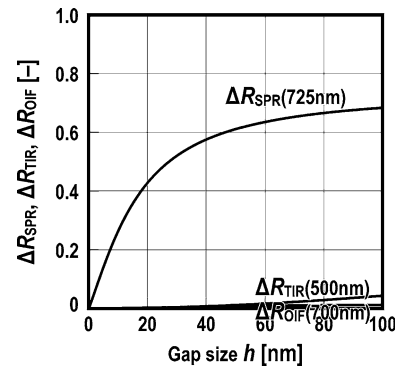
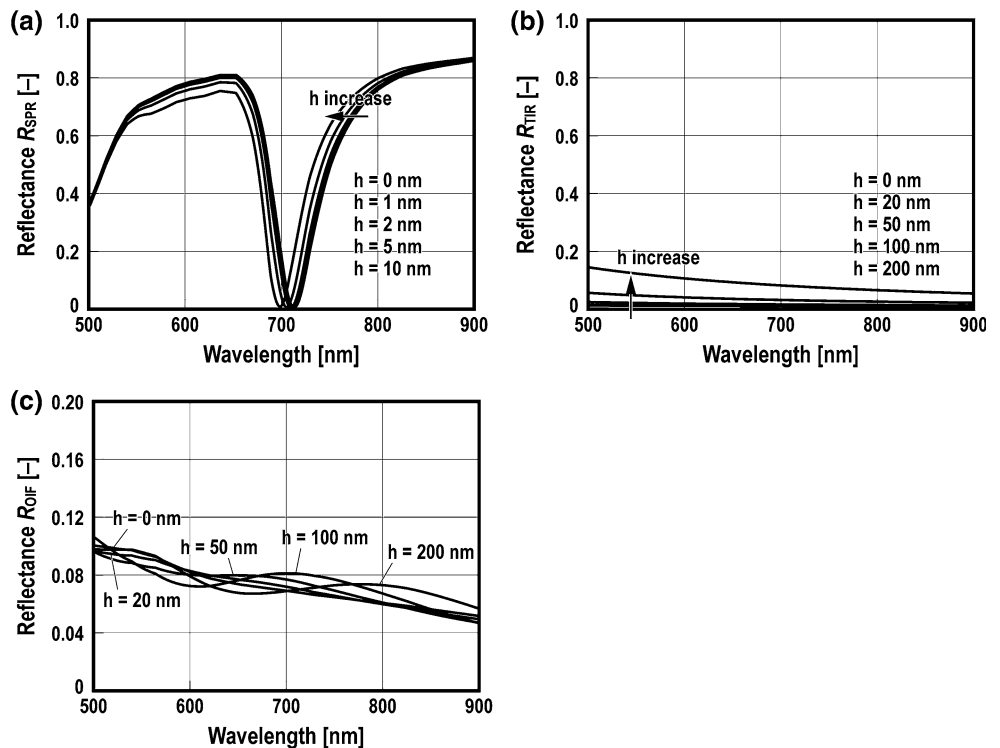


Fig. 11 Changes in $\Delta R_{SPR}(725\text{ nm})$, $\Delta R_{TIR}(500\text{ nm})$, and $\Delta R_{OIF}(700\text{ nm})$, associated with values of h for contact between the PDMS and the flat plane via a water gap

R_{SPR} for $k = 0.1$ is quite different from that for $k = 0$. The sharp minima observed in the typical SPR spectra shown in Fig. 6 are not observed in Fig. 13. On the other hand, for the TIR and OIF methods, there is not a large difference between the spectra of Figs. 6 and 13. Focusing on the difference between the slopes of ΔR_{SPR} in Figs. 7 and 14, the sensitivity of the SPR method with a non-transparent material is much lower than with transparent material. From the results, it was found that the SPR method will be effective in experiments only when an optically transparent elastomer is used. When a non-transparent elastomer must be used, the TIR method is the most effective for measurement of real-contact area.

Fig. 10 Water gap results: the wavelength dependence of R_{SPR} , R_{TIR} , and R_{OIF} for contact between the PDMS and a flat plane via a water gap: **a** SPR method; **b** TIR method; **c** OIF method



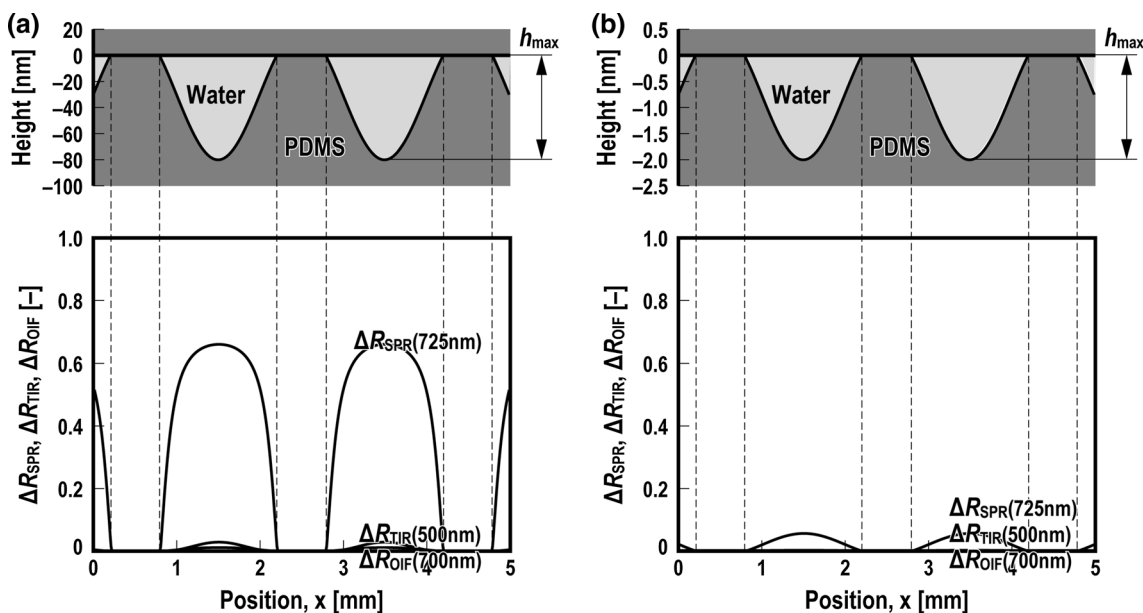
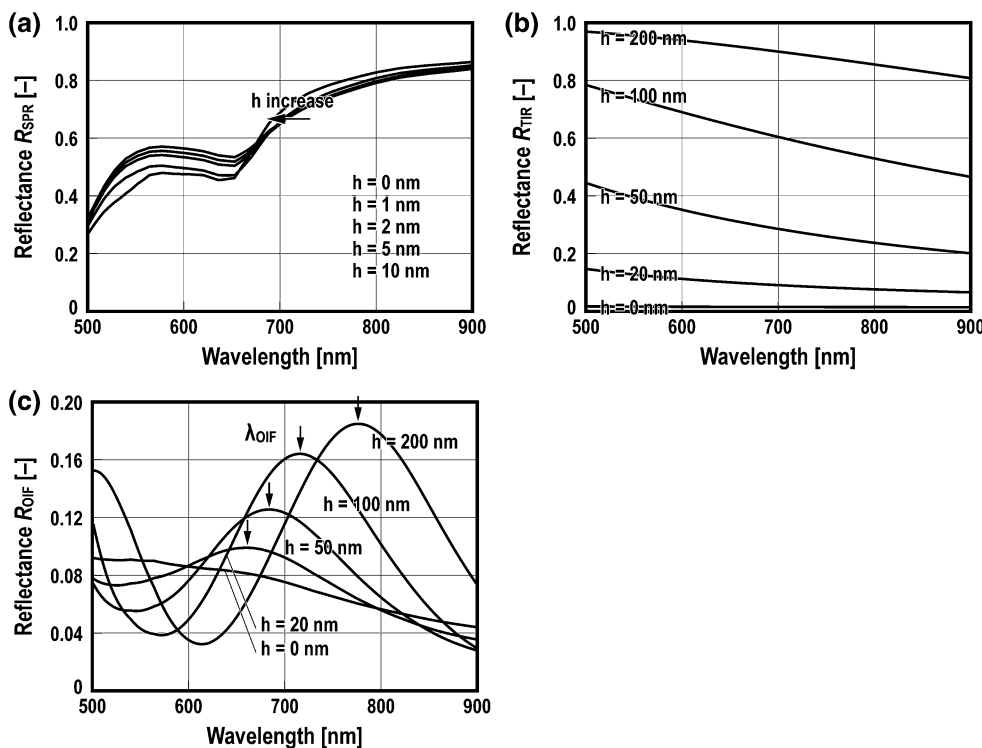


Fig. 12 Model calculations for the spatial distribution of ΔR_{SPR} , ΔR_{TIR} , and ΔR_{OIF} when the rough surface of an optically transparent elastomer is in contact with a flat rigid plane via a water gap: **a** maximum gap of 80 nm between the flat and the elastomer surfaces; **b** maximum gap is 2 nm

Fig. 13 Non-transparent elastomer: wavelength dependence of R_{SPR} , R_{TIR} , and R_{OIF} for contact between an optically non-transparent elastomer ($k = 0.1$) and a flat plane via an air gap: **a** SPR method; **b** TIR method; **c** OIF method



5.4 Feasibility of the SPR Method

The high sensitivity of the SPR method for detecting non-contact regions separated by a small air gap (or water gap) was demonstrated through numerical simulations. The high-sensitivity results from the SPR response's high

sensitivity to a small change in the effective refractive index near the reflection plane. For example, a typical SPR sensor can measure a refractive index change smaller than 10^{-5} . In general, the limit of detection for a dielectric layer on a metal surface is approximately 0.1 nm thickness [31].

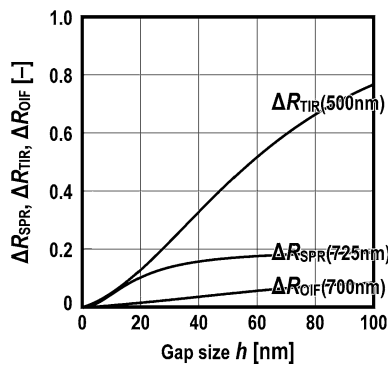


Fig. 14 Changes in reflectance $\Delta R_{\text{SPR}}(725 \text{ nm})$, $\Delta R_{\text{TIR}}(500 \text{ nm})$, and $\Delta R_{\text{OIF}}(700 \text{ nm})$, associated with the gap size h , for contact between the optically non-transparent elastomer ($k = 0.1$) and the flat plane via an air gap

As far as the authors know, this study is the first to consider applying the SPR method to direct the observation of a real-contact area. From the model calculations, a high feasibility was demonstrated; the SPR method can detect non-contact regions with an air gap as small as a few nm thickness. It can provide temporal and spatial observations of real-contact distributions without complicated calibrations or analysis. Here, the horizontal space resolution depends on the optical system used. In addition, it should be noted that the SPR method has high scalability; for example, the two-color SPR method [32], the multi-solvent SPR method [33], SPR-enhanced Raman measurement [34], and SPR-enhanced ellipsometry [35], have been

developed to acquire more accurate and complete information. Therefore, the application of these SPR techniques to contact surface observation can provide a fruitful direction for studying the mechanisms at play in the contact dynamics and friction of soft materials.

It should be noted that the results presented in this study are based on model calculations for assumed material and geometric conditions. For example, the sensibility of the SPR method strongly depends on the incident angle θ and the optical properties of the prism. Of course, the optical properties of the elastic materials are among the most important parameters that determine the sensitivity of these methods. There are additional variations for all the optical methods to improve their sensitivity, e.g., polarization analysis. Therefore, to make a more thorough quantitative comparison, more calculation and analysis are required. However, the aim of this study was to demonstrate a high feasibility for developing a method based on SPR. Therefore, further calculations would be outside the main scope of this study, but a next step in developing an SPR microscope for the investigation of contact phenomena.

6 Conclusion

This study presented a novel method for distinguishing contact and non-contact areas distributed within a region of apparent contact between a rough elastomer surface and a rigid flat plane. The method focuses on the observation of surface plasmon resonances (SPR), using the Kretschmann

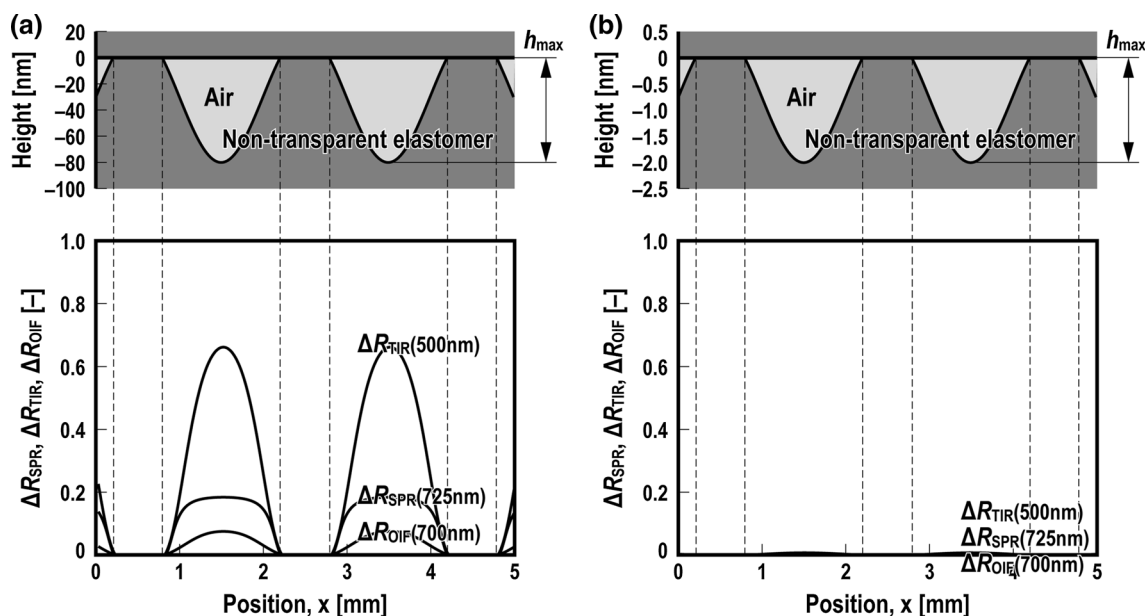


Fig. 15 Model calculations for the spatial distribution of ΔR_{SPR} , ΔR_{TIR} , and ΔR_{OIF} when the rough surface of an optically non-transparent elastomer is contacting on a flat rigid plane with an air

gap: **a** maximum gap between the flat and the elastomer surfaces is 80 nm; **b** maximum gap is 2 nm

configuration. Through numerical calculations, it is shown that the SPR method can detect air gap (or water gap) with a few nm thickness in the apparent contact area by the measurement of reflected light intensity. Thus, the SPR method can provide the visualization of the spatial distribution of real-contact regions within the apparent contact area without complicated calibrations. Although the SPR method has some limitations as described in this report, the direct measurement of the area of real contact and the gap thickness will provide a fruitful information for studying the mechanisms of contact dynamics and friction for soft materials.

References

- Liang, X., Linquing, Z.: A new method for the experimental investigation of contact in mixed lubrication. *Matter* **132**, 221–233 (1989)
- Eguchi, M., Shibamiya, T., Yamamoto, T.: Dynamic strain measurements in a sliding microstructured contact. *J. Phys. Condens. Matter* **20**, 015004 (2008)
- Eguchi, M., Shibamiya, T., Yamamoto, T.: Measurement of real contact area and analysis of stick/slip region. *Tribol. Int.* **42**, 1781–1791 (2009)
- Soneda, T., Nakano, K.: Investigation of vibrotactile sensation of human fingerpads by observation of contact zones. *Tribol. Int.* **43**, 210–217 (2010)
- Krick, B.A., Hahn, D.W., Sawyer, W.G.: Optical in situ micro tribometer for analysis of real contact area for contact mechanics, adhesion, and sliding friction. *Tribol. Lett.* **45**, 185–194 (2012)
- Nitta, I., Tsukiyama, Y., Tsukada, T., Terao, H.: Measurement of real contact area on thermal print head using a laser microscope with a wide field of view. *Tribol. Int.* **79**, 162–173 (2014)
- Eason, E.V., Hawkes, E.W., Windheim, M., Christensen, D.L., Libby, T., Cutkosky, M.R.: Stress distribution and contact area measurements of a gecko toe using a high-resolution tactile sensor. *Bioinspir. Biomim.* **10**, 016013 (2015)
- Matsuda, K., Hashimoto, D., Nakamura, K.: Real contact area and friction property of rubber with two-dimensional regular wavy surface. *Tribol. Int.* **93**, 523–529 (2016)
- Holm, R.: *Electric Contacts Handbook*. Springer, Berlin (1958)
- Nakano, K., Akiyama, Y.: Simultaneous measurement of thickness and coverage of loaded boundary films with complex impedance analysis. *Tribol. Lett.* **22**, 127–134 (2006)
- Manabe, K., Nakano, K.: Breakdown of oil films and formation of residual films. *Tribol. Int.* **41**, 1103–1113 (2008)
- Dwyer-Joyce, R.S., Reddyhoff, T., Drinkwater, B.W.: Operating limits for acoustic measurement of rolling bearing oil film thickness. *Tribol. Trans.* **47**, 127–134 (2004)
- Dwyer-Joyce, R.S., Reddyhoff, T., Zhu, J.: Ultrasonic measurement for film thickness and solid contact in elastohydrodynamic lubrication. *J. Tribol.* **133**, 031501 (2011)
- Rubinstein, S.M., Cohen, G., Fineberg, J.: Dynamics of precursors to frictional sliding. *Phys. Rev. Lett.* **98**, 226103 (2007)
- Maegawa, S., Suzuki, A., Nakano, K.: Precursors of global slip in a longitudinal line contact under non-uniform normal loading. *Tribol. Lett.* **38**, 313–323 (2010)
- Schallamach, A.: How does rubber slide? *Wear* **17**, 301–302 (1971)
- Maegawa, S., Nakano, K.: Mechanism of stick-slip associated with Schallamach waves. *Wear* **268**, 924–930 (2010)
- Maegawa, S., Itoigawa, F., Nakamura, T.: Dynamics in sliding friction of soft adhesive elastomer: Schallamach waves as a stress-relaxation mechanism. *Tribol. Int.* **96**, 23–30 (2016)
- Maegawa, S., Yamaguchi, J., Itoigawa, F., Nakamura, T.: Discussion on surface plasmon resonance technique in the Otto configuration for measurement of lubricant film thickness. *Tribol. Lett.* **62**, 14 (2016)
- Otto, A.: Excitation of nonradiative surface plasma waves in silver by the method of frustrated total reflection. *Z. Phys.* **216**, 398–410 (1968)
- Kretschmann, E.: The determination of the optical constants of metals by excitation of surface plasmons. *Z. Phys.* **241**, 313–324 (1971)
- Raether, H.: *Surface plasmons on smooth and rough surfaces and on gratings*. Springer, Berlin (1988)
- Jung, L.S., Campbell, C.T., Chinowsky, T.M., Mar, M.N.: Quantitative interpretation of the response of surface plasmon resonance sensors to adsorbed films. *Langmuir* **14**, 5636–5648 (1998)
- Heavens, O.S.: *Optical Properties of Thin Solid Films*. Dover Publications, New York (1991)
- Born, M., Wolf, E.: *Principle of Optics, Electromagnetic Theory of Propagation, Interference and Diffraction of Light*, 6th edn. Cambridge University Press, Cambridge (1997)
- Macleod, H.A.: *Thin-film Optical Filters*, 3rd edn. Institute of Physics Publishing, Bristol (2001)
- Fu, Z., Guo, F., Wong, P.L.: Theoretical study on the interferometry of thin EHL film measurement. *Tribol. Lett.* **31**, 57–65 (2008)
- <http://www.filmetricsinc.jp/refractive-index-database/>
- Cudek, V., Krupka, I., Hartl, M.L.: Application of spectroscopic reflectometry to elastohydrodynamic lubrication film study. *Tribol. Lett.* **45**, 195–205 (2012)
- Maegawa, S., Koseki, A., Itoigawa, F., Nakamura, T.: In situ observation of adsorbed fatty acid films under shearing condition using surface plasmon resonance. *Tribol. Int.* **97**, 228–233 (2016)
- Haeussling, L., Ringsdorf, H., Schmitt, F.J., Knoll, W.: Biotin-functionalized self-assembled monolayers on gold: surface plasmon optical studies of specific recognition reactions. *Langmuir* **7**, 1837–1840 (1991)
- Peterlinz, K.P., Georgiadis, R.C.: Two-color approach for determination of thickness and dielectric constant of thin films using surface plasmon resonance spectroscopy. *Opt. Commun.* **130**, 260–266 (1996)
- Bruijn, H.E.B., Altenburg, B.S.F., Kooyman, R.P.H., Greve, J.: Determination of thickness and dielectric constant of thin transparent dielectric layers using surface plasmon resonance. *Opt. Commun.* **82**, 425–432 (1991)
- Le Ru, E.C., Etchegoin, P.G.: *Principles of Surface Enhanced Raman Spectroscopy and Related Plasmonic Effects*. Elsevier, Amsterdam (2009)
- Westphal, P., Bornmann, A.: Biomolecular detection by surface plasmon enhanced ellipsometry. *Sens. Actuators B* **84**, 278–282 (2002)